TOPOLOGY OPTIMIZATION OF THREE DIMENSIONAL STRUCTURES SUBJECT TO SELF-WEIGHT LOADING

J. M. M. LUZ FILHO AND A. A. NOVOTNY

Abstract. Topology optimization of structures under self-weight loading is a challenging problem which has received increasing attention in the last years. The use of standard formulations based on compliance minimization under volume constraint suffers from numerous difficulties for self-weight dominant scenarios, such as non-monotonic behaviour of the compliance, possible unconstrained character of the optimum and parasitic effects for low densities in density-based approaches. In order to overcome the first two issues, a regularized formulation of the classical compliance minimization problem under volume constraint is adopted, which enjoys two important features: (a) it allows for imposing any feasible volume constraint and (b) the standard (original) formulation is recovered once the regularizing parameter vanishes. The resulting topology optimization problem is solved with the help of the topological derivative method, which naturally overcomes the last issue, since no intermediate densities (grey-scale) approach is necessary. Finally, in order to show the effectiveness of the proposed approach, a set of benchmark examples into three spatial dimensions is presented, which are: (1) a bridge structure under pure self-weight loading; (2) a truss-like structure subject to both, self-weight loading and external forces acting co-linearly and in orthogonal directions and (3) a tower structure under external loads and dominant self-weight loading.

1. Introduction

Topology optimization of structures has been a subject of intense research over the last decades. The main goal of topology optimization is to find a material distribution within a design domain which minimizes a given shape functional. Since the pioneering paper by Bendsøe and Kikuchi (1988), many approaches have been proposed and successfully applied to solve the classical compliance minimization under volume constraint problem of structures subject to external loads. On the other hand, the much more challenging problem of topology optimization of structures under self-weight loading remains a topic of great interest as the use of standard formulations based on the compliance minimization under volume constraint are not suitable for this scenario. More precisely, the use of such formulations leads to several difficulties once the structure's self-weight becomes dominant, such as non-monotonic behaviour of the compliance, possible unconstrained character of the optimum and parasitic effects for low densities for density-based models, as pointed out by Bruyneel and Duysinx (2005).

Despite the large amount of works in the context of structural optimization, most developments in this field are concerned with structural compliance minimization under volume constraint and fixed external independent loads. Surprisingly, only a few published works address topology optimization of structures subject to self-weight loading, despite the important role played by body forces in many engineering applications. In this sense, let us trace a brief overview of the developments proposed so far to deal with this problem. Initially, in order to alleviate the parasitic effects when using density-based models, Bruyneel and Duysinx (2005) propose a modified discontinuous SIMP model (Solid Isotropic Material Penalization) together with a novel approach combining the Method of Moving Asymptotes (MMA) with the Gradient Based Method. In the context of evolutionary approaches, Ansola et al. (2006) applied a modified Evolutionary Structural Optimization (ESO), in which the convergence of the algorithm is enhanced by introducing a correction factor to the sensitivities, whereas Huang and Xie (2011) proposed a modified Bi-directional ESO (BESO) method with the Rational Approximation of Material Properties (RAMP) model. Alternatively, Xu et al. (2013) propose the guide-weight approach using the optimality criterium method, and also compares the performance between SIMP and RAMP in solving body force problems. The work by Chang and Chen (2014) aims

Date: April 30, 2024.

Key words and phrases. Structural topology optimization, self-weight loading, topological derivative method.

to apply the Gradient Projection Method (GPM) to topology optimization including density-dependent force, which is solved as a general nonlinear programming problem. Finally, the works by Kumar (2022) and Garaigordobil et al. (2022) represent the most recent developments in topology optimization of structures subject to self-weight loading. In Kumar (2022), a density-based approach grounded in a novel mass density interpolation strategy using a smooth Heaviside function is proposed, aiming for a continuous transition between solid and void states of elements. Finally, the work by Garaigordobil et al. (2022) proposes the integration of topology optimization procedures and additive manufacturing techniques with overhang constraints.

In contrast to the aforementioned approaches, the recent paper by Novotny et al. (2021) proposes a novel regularized formulation for the compliance minimization under volume constraint problem of structures subject to self-weight loading. The non-suitability of the standard formulation is confirmed by Novotny et al. (2021) through a simple analysis of a one dimensional bar subject to self-weight loading, showing that its use leads to trivial solutions in the case of pure self-weight loading, by removing all the material. In this sense, the regularized version of the standard compliance minimization problem under volume constraint from Novotny et al. (2021) aims to avoid such trivial solutions and, therefore, allows for imposing any feasible volume constraint. Roughly speaking, the introduction of the so-called regularizing term to the problem formulation allows for characterizing a non-trivial local minimizer. In addition, the parasitic effects associated with low densities designs reported in Bruyneel and Duysinx (2005) are naturally avoided in Novotny et al. (2021) by the use of the topological derivative concept combined with a level-set domain representation method. In fact, the topological derivative method has been originally designed to deal with structural topology optimization (Sokołowski and Żochowski, 1999; Garreau et al., 2001), by giving a precise and quantitative information on the sensitivity of structural responses with respect to topological domain perturbations, such as nucleation of small holes. Hence, no intermediate densities (grey-scale) approach is necessary.

Therefore, our main purpose in this paper is to extend the work by Novotny et al. (2021) to the topology optimization of self-weight loading structures into three spatial dimensions. We stress however that this extension is non-trivial since the associated topological derivative of the structural compliance accounting for body forces is not fully available in the literature and thus has to be deduced. In particular, the contribution of the body force itself has not been considered yet in the case of three-dimensional elasticity. Hence, the topological derivative with respect to the nucleation of spherical inclusions endowed with different material properties from the background governed by a contrast parameter is rigorously derived. The asymptotic formulas are justified by *a priori* estimates of the remainders with the help of the compound asymptotic analysis method fully developed in the book by Maz'ya et al. (2000). See also the books by Dalla Riva et al. (2021), Ammari and Kang (2004) and Ammari et al. (2013a). In addition, the obtained results are presented in their limit cases with respect to the contrast parameter, leading to closed "plug-and-play" formulae that are easy to interpret and implement, which represents the main theoretical contribution of the paper. Actually, the obtained formulae are useful not only for solving the problem we are dealing with, but also to many other relevant applications governed by energy-like shape functional, such as structural eigen-value problems, imaging of structural defects, synthesis of elastic microstructures and design of compliant mechanisms, for instance. Finally, in order to show the effectiveness of the proposed approach, some benchmark examples into three spatial dimensions are presented, which are: (1) a bridge structure under pure self-weight loading; (2) a truss-like structure subject to both, self-weight loading and external forces acting co-linearly and in orthogonal directions and (3) a tower structure under external loads and dominant self-weight loading.

The paper is organized as follows. In Section 2 the optimization problem we are dealing with is introduced. The topological derivative method is presented in Section 3. The topological asymptotic analysis of the compliance shape functional with respect to nucleation of spherical inclusions is relegated to the Appendix A. The topology optimization algorithm based on the resulting topological derivative and a level-set domain representation method is explained in details through Section 3.1. In Section 3.2, relevant computational aspects of the FreeFEM implementation are discussed. Some numerical experiments are presented in Section 4, showing the effectiveness of the proposed approach. Finally, the paper ends with some concluding remarks in Section 5.

2. Problem Formulation

Let us consider an open and bounded domain $\mathcal{D} \subset \mathbb{R}^3$ with Lipschitz boundary denoted as $\Gamma := \partial\mathcal{D}$. The boundary Γ is the union of two given non-overlapping subsets Γ_D and Γ_N, that is $\Gamma = \overline{\Gamma}_D \cup \overline{\Gamma}_N$ and $\Gamma_D \cap \Gamma_N = \varnothing$, where Γ_D and Γ_N are Dirichlet and Neumann boundaries, respectively. See sketch in Figure 1.

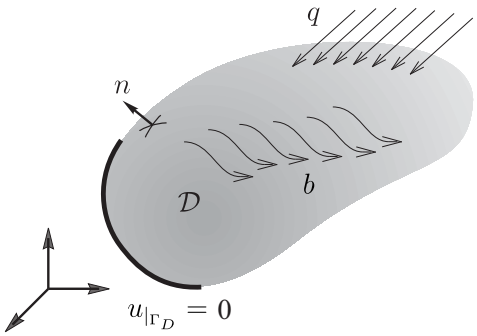

Figure 1. The elasticity problem.

We are interested in the minimum compliance problem of self-weight loading structures under volume constraint. Since this problem leads to the trivial solution as the self-weight becomes dominant, the regularized formulation proposed in Novotny et al. (2021) is adopted, which enjoys two important features: (a) it allows for imposing any feasible volume constraint and (b) the standard (original) formulation is recovered once the regularizing parameter vanishes. Such a problem consists in finding a subdomain $\Omega \subset \mathcal{D}$ that solves the following minimization problem:

$$\begin{cases} \underset{\Omega\subset\mathcal{D}}{\text{Minimize}}\ \mathcal{F}^{\alpha}_{\Omega}(u) := \mathcal{C}(u) + \alpha|\Omega|^{-1}\ , \\ \text{Subject to } |\Omega| \leq M, \end{cases} \tag{2.1}$$

where the quantity $M > 0$ is the volume constraint, $0 \leq \alpha < \infty$ is the so-called regularizing parameter and $\mathcal{C}(u)$ is the structural compliance, given by

$$\mathcal{C}(u) = \int_{\Gamma_N} q \cdot u + \int_{\mathcal{D}} b \cdot u\ , \tag{2.2}$$

with q the prescribed traction on Γ_N. The vector displacement field u is the solution of the following variational problem: Find $u \in \mathcal{U}$, such that:

$$\int_{\mathcal{D}} \sigma(u) \cdot (\nabla\eta)^s = \int_{\mathcal{D}} b \cdot \eta + \int_{\Gamma_N} q \cdot \eta\ , \quad \forall \eta \in \mathcal{V}\ , \tag{2.3}$$

where the stress tensor $\sigma(u)$ and the self-weight b are, respectively, given by

$$\sigma(u) = \delta\mathbb{C}(\nabla u)^s \quad \text{and} \quad b = \delta b_0\ , \tag{2.4}$$

with the constant vector b_0 representing a reference body force. The spaces $\mathcal{U}$ and $\mathcal{V}$ are defined as

$$\mathcal{U} = \mathcal{V} = \{\varphi \in H^1(\mathcal{D}) : \varphi_{|\Gamma_D} = 0\}\ . \tag{2.5}$$

The statement of the problem is complemented with the definition of the following piece-wise constant functions

$$\delta(x) := \begin{cases} 1, & \text{if } x \in \Omega\,, \\ \delta_0, & \text{if } x \in \mathcal{D} \setminus \Omega\,, \end{cases} \tag{2.6}$$

with $0 < \delta_0 \ll 1$ representing a very weak/light phase used to mimic voids. Finally, the strong system associated with the variational problem (2.3) can be stated as: Find u, such that

$$\begin{cases} \text{div}\sigma(u) &=& b & \text{in } \mathcal{D}\ , \\ \sigma(u) &=& \delta\mathbb{C}(\nabla u)^s & \\ u &=& 0 & \text{on } \Gamma_D\ , \\ \sigma(u)n &=& q & \text{on } \Gamma_N\ . \end{cases} \tag{2.7}$$

In this paper, the topological derivative method is used for solving the optimization problem (2.1), which is presented in the next section.

3. Topological derivative method

The topological derivative is defined as the first term of the asymptotic expansion of a given shape functional with respect to a small parameter that measures the size of singular domain perturbations, such as holes, inclusions, source-terms and cracks. In other words, the topological derivative measures the sensitivity of the associated shape functional with respect to the nucleation of a singular domain perturbation. This concept can naturally be used as a steepest-descent direction in an optimization process like in any method based on the gradient of the cost functional. Thus, the topological derivative method has applications in many different fields. For a complete review of the topological derivative method and the most recent developments in this area, see the special issue on the topological derivative method and its applications in computational engineering recently published in the Engineering Computations Journal (Novotny et al., 2022), covering various topics ranging from new theoretical developments (Amstutz, 2022; Baumann and Sturm, 2022; Delfour, 2022) to applications in structural and fluid dynamics topology optimization (Kliewe et al., 2022; Romero, 2022; Santos and Lopes, 2022), geometrical inverse problems (Bonnet, 2022; Canelas and Roche, 2022; Fernandez and Prakash, 2022; Louër and Rapún, 2022a,b), synthesis and optimal design of metamaterials (Ferrer and Giusti, 2022; Yera et al., 2022), fracture mechanics modelling (Xavier and Van Goethem, 2022), up to industrial applications (Rakotondrainibe et al., 2022) and experimental validation of the topological derivative method (Barros et al., 2022).

In this work, the parameter δ from (2.6) induces a very weak/light phase for mimicking voids, which allows for working in a fixed computational domain. Therefore, the topological derivative associated with the shape functional $\mathcal{F}^{\alpha}_{\Omega}(u)$ from (2.1) is here stated in its limit cases versions when a small portion of material is either removed or added to the design domain, namely:

Theorem 1. *The topological derivative of the shape functional $\mathcal{F}^{\alpha}_{\Omega}(u)$ from (2.1), with respect to the nucleation of a small spherical inclusion endowed with different material property from the background, may be written as the sum of the topological derivative of the compliance shape functional and the topological derivative associated with the regularizing term, namely*

$$D_T\mathcal{F}^{\alpha}_{\Omega}(x) = D_T\mathcal{C}(x) - \alpha|\Omega|^{-2}D_T|\Omega|(x)\ . \tag{3.1}$$

***Case A**. Let us consider $x \in \Omega$. In this case, a small portion of material is removed from Ω. Then the topological derivative $D_T\mathcal{C}$ reads*

$$D_T\mathcal{C} = \mathbb{P}_0\sigma(u)\cdot(\nabla u)^s - 2b_0\cdot u\ , \tag{3.2}$$

with the polarization tensor $\mathbb{P}_0$ written as

$$\mathbb{P}_0 = \frac{3}{2}\frac{1-\nu}{7-5\nu}\left(10\mathbb{I} - \frac{1-5\nu}{1-2\nu}\mathrm{I}\otimes\mathrm{I}\right)\ . \tag{3.3}$$

In addition, the topological derivative $D_T|\Omega|$ is simply given by

$$D_T|\Omega| = -1\ . \tag{3.4}$$

***Case B**. Let us consider $x \in \mathcal{D}\setminus\Omega$. In this case, a small portion of material is added within $\mathcal{D}\setminus\Omega$. Then the topological derivative $D_T\mathcal{C}$ is given by*

$$D_T\mathcal{C} = \mathbb{P}_\infty\sigma(u)\cdot(\nabla u)^s + 2b_0\cdot u\ , \tag{3.5}$$

with the polarization tensor $\mathbb{P}_\infty$ written as

$$\mathbb{P}_\infty = -\frac{3}{2}\frac{1-\nu}{4-5\nu}\left(5\mathbb{I} + \frac{1-5\nu}{1+\nu}\mathrm{I}\otimes\mathrm{I}\right)\ . \tag{3.6}$$

Finally, the topological derivative $D_T|\Omega|$ is given by

$$D_T|\Omega| = +1\ . \tag{3.7}$$

Proof. Since the regularizing term does not depend on the state u, its topological derivative is trivially obtained. In contrast, the topological derivative calculation of the compliance shape functional is much more involved and will be rigorously presented in the Appendix A. □

3.1. **Topology optimization algorithm.** In this section, we provide a brief description of the topology optimization algorithm based on the topological derivative combined with a level-set domain representation method as proposed by Amstutz and Andrä (2006). The topology optimization problem (2.1) is conveniently rewritten as

$$\left\{ \begin{array}{l} \underset{\Omega\subset\mathcal{D}}{\text{Minimize}}\ J^{\alpha}(\Omega) := \dfrac{J(\Omega)}{J(\mathcal{D})} + \alpha \left(\dfrac{|\Omega|}{|\mathcal{D}|} \right)^{-1} , \\ \text{Subject to } |\Omega| \leq M, \end{array} \right. \tag{3.8}$$

where $J(\Omega) = \mathcal{C}(u)$ and $J(\mathcal{D}) = \mathcal{C}(u_0)$, with u and u_0 solutions to (2.3) for $\Omega \subset \mathcal{D}$ and $\Omega \equiv \mathcal{D}$, respectively. The quantities $J(\Omega)/J(\mathcal{D})$ and $|\Omega|/|\mathcal{D}|$ are referred to as relative compliance and volume fraction, respectively. The idea consists in achieving a local optimality condition for the minimization problem (3.8), given in terms of the topological derivative and a level-set function. Furthermore, the domain $\Omega \subset \mathcal{D}$ and the complement $\mathcal{D} \setminus \Omega$ are characterized by a level-set function Ψ of the form

$$\Omega = \{x \in \mathcal{D} : \Psi(x) < 0\} \quad \text{and} \quad \mathcal{D} \setminus \Omega = \{x \in \mathcal{D} : \Psi(x) > 0\} , \tag{3.9}$$

where Ψ vanishes on the interface between Ω and $\mathcal{D}\setminus\Omega$. A local sufficient optimality condition for problem (3.8), under the considered class of domain perturbation given by spherical inclusions, can be stated as (Amstutz, 2011)

$$D_T J^{\alpha}(x) > 0 \quad \forall x \in \mathcal{D} . \tag{3.10}$$

In this sense, let us define the quantity

$$g(x) := \left\{ \begin{array}{ll} -D_T J^{\alpha}, & \text{if } \Psi(x) < 0 , \\ +D_T J^{\alpha}, & \text{if } \Psi(x) > 0 , \end{array} \right. \tag{3.11}$$

which allows for rewriting the condition (3.10) as follows

$$\left\{ \begin{array}{ll} g(x) < 0, & \text{if } \Psi(x) < 0 , \\ g(x) > 0, & \text{if } \Psi(x) > 0 . \end{array} \right. \tag{3.12}$$

Note that (3.12) is satisfied, where the quantity g coincides with the level-set function Ψ up to a strictly positive factor, namely $\exists\, \tau > 0 : g = \tau\Psi$, or equivalently

$$\theta := \arccos \left[\frac{\langle g, \Psi \rangle_{L^2(\mathcal{D})}}{\|g\|_{L^2(\mathcal{D})} \|\Psi\|_{L^2(\mathcal{D})}} \right] = 0 , \tag{3.13}$$

which shall be used as the optimality condition in the topology design algorithm, where θ is the angle between the functions g and Ψ in $L^2(\mathcal{D})$.

Now, with all the elements presented so far, we are in condition to explain the algorithm. We start by choosing an initial level-set function Ψ_0. In a generic iteration i, we compute the function g_i associated with the level-set function Ψ_i. Then, the new level-set function Ψ_{i+1} is updated according to the following linear combination of the functions g_i and Ψ_i

$$\Psi_0 : \|\Psi_0\|_{L^2(\mathcal{D})} = 1 , \tag{3.14}$$

$$\Psi_{i+1} = \frac{1}{\sin\theta_i} \left[\sin((1-w)\theta_i) + \sin(w\theta_i) \frac{g_i}{\|g_i\|_{L^2(\mathcal{D})}} \right] \quad \forall i \in \mathbb{N} , \tag{3.15}$$

where θ_i is the angle between g_i and Ψ_i, and w is a step size determined by a linear search performed to decrease the value of the objective function J_i^{α} associated with Ψ_i. The process ends when the condition $\theta_i \leq \epsilon_\theta$ is satisfied at some iteration, where ϵ_θ is a given small numerical tolerance. If at some iteration the line-search step size w is found to be smaller than a given numerical tolerance $\epsilon_w > 0$ and the local optimality condition is not satisfied, that is $\theta_i > \epsilon_\theta$, then an adaptive mesh refinement is performed and the iterative process is carried on.

3.2. **Computational implementation aspects.** The topology optimization algorithm presented in Section 3.1 is implemented in FreeFEM, an open-source program written in C++ for solving partial differential equations by the finite element method (Hecht). In fact, FreeFEM was developed to easily handle the complex processes required for finite element analysis with a few commands, and it is compatible with many external libraries, such as ARPACK, Gmsh, Mmg, Paraview, and PETSc, for instance. Thus, FreeFEM presents many interesting and useful features, such as a remarkable resemblance of the mathematical and computational languages and an almost straightforward extension to three spatial dimensions of implementations originally written for two dimensional problems. Thanks to this last feature, the FreeFEM implementation for the topology design optimization of structures into two spatial dimensions submitted to external loads, recently reported in the educational paper by Filho et al. (2023), can be easily extended, from a computational perspective, to the topology optimization problem of three dimensional structures subject to self-weight loading we are dealing with. Although FreeFEM offers a parallel version based on the domain decomposition method and PETSc library for the linear algebra backend, the present implementation is completely analogous to the one provided in Filho et al. (2023) and relies on the use of direct solvers. In this sense, we present some sample codes with the main changes necessary to extend the referred code to three spatial dimensions and to include the self-weight loading contribution. More precisely, these sample codes focus mainly in generating and discretizing the initial design domain, solving the elasticity system, computing the topological derivative field and performing the adaptive mesh refinement. Those sample codes represent the major changes to be done in the reference code provided in Filho et al. (2023). In fact, only small changes are required in the optimization process in order to adapt it to the present case, such as computing the compliance shape functional and the volume as well as the associated topological derivative at each iteration. Regarding the construction of the initial design domain, FreeFEM provides simple mesh generation functions such as the command `cube`. In this step, characterizing the mesh boundaries with the appropriate labels is crucial for correctly imposing the boundary conditions and later solving the elasticity system. In this sense, Table 1 presents the labels associated with different boundary condition types adopted herein.

TABLE 1. Boundary labels

Label	Corresponding boundary condition
1	Dirichlet homogeneous
2	Neumann non-homogeneous (surface traction)
3	symmetry in the x_1 direction
4	symmetry in the x_2 direction

The topology optimization implementation provided in Filho et al. (2023) explores the powerful feature of macros, specially for computing the topological derivative field and for solving the elasticity problem. Macros not only make names shorter but also avoid runtime overheads. In simple terms, a macro is a piece of code in a program that is replaced by the value of the macro. Whenever a macro name is encountered by the compiler, it replaces the name with the definition of the macro. In this sense, the topological derivative of the compliance shape functional at the bulk (3.2) and weak (3.5) phases is respectively given by the macros `dte(u)` and `dti(u)` with the self-weight contribution given in macro `bb(u)`. Moreover, in Listing 1 `psi` and `chi` are, respectively, the level-set and characteristic function of the bulk phase, `chigamma` represents the material distribution, `E` is the Young's modulus, `nu` the Poisson ratio and `la` and `mu` are the Lamé's coefficients. Therefore, the descent direction $g(x)$ given by expression (3.11) is translated to FreeFEM language as `g = -chi*dte(u) + (1-chi)*dti(u)`, as shown in the last line of the following sample code.

LISTING 1. The use of macros for computing the topological derivative field.

```
// Coefficients to compute the topological derivative
real coef0E = (3.0/2.0)*((1.0 - nu)/(7.0 - 5.0*nu)), coef1E = coef0E*10.0, coef2E = coef0E*((5.0*nu - 1.0)
    ↪ /(1.0 - 2.0*nu));
```

```
real coef0I = (3.0/2.0)*((1.0 - nu)/(4.0 - 5.0*nu)), coef1I = -5.0*coef0I, coef2I = coef0I*((5.0*nu - 1.0)
    ↪ /(1.0 + nu));
// Macros
macro def(i)[i,i#y,i#z] //EOM
macro init(i)[i, i, i] //EOM
macro div(u) (dx(u) + dy(u#y) + dz(u#z)) // EOM
macro e11(u) (dx(u)) // EOM
macro e22(u) (dy(u#y)) // EOM
macro e33(u) (dz(u#z)) // EOM
macro e12(u) ((dy(u)+dx(u#y))/2.0) // EOM
macro e13(u) ((dz(u)+dx(u#z))/2.0) // EOM
macro e23(u) ((dy(u#z)+dz(u#y))/2.0) // EOM
macro s11(u) (chigamma*(la*div(u) + 2.0*mu*e11(u))) // EOM
macro s22(u) (chigamma*(la*div(u) + 2.0*mu*e22(u))) // EOM
macro s33(u) (chigamma*(la*div(u) + 2.0*mu*e33(u))) // EOM
macro s12(u) (chigamma*(2.0*mu*e12(u))) // EOM
macro s13(u) (chigamma*(2.0*mu*e13(u))) // EOM
macro s23(u) (chigamma*(2.0*mu*e23(u))) // EOM
macro trs(u) (s11(u) + s22(u) + s33(u)) // EOM
macro se(u) (s11(u)*e11(u) + s22(u)*e22(u) + s33(u)*e33(u) + 2.0*(s12(u)*e12(u) + s13(u)*e13(u) + s23(u)*
    ↪ e23(u))) //
macro bb(u) (-2.0*rho*gravity*uz) // EOM
macro dte (u) (coef1E*se(u) + coef2E*trs(u)*div(u) - bb(u))// EOM
macro dti (u) (coef1I*se(u) + coef2I*trs(u)*div(u) + bb(u))// EOM
// Computing function g (descent direction)
chi = (psi < 0);
g = -chi*dte(u) + (1 - chi)*dti(u);
```

For solving the elasticity system into three spatial dimensions in FreeFEM, only a few changes are necessary when compared to the two-dimensional case provided in Filho et al. (2023). One should notice that the boundary labels described in Table 1 are also adopted in Listing 2 to solve elasticity system. In addition, the weak formulation given in (2.3) is easily translated to FreeFEM language as shown in Listing 2, highlighting the similarities between the mathematical and FreeFEM computational language. Finally, the elasticity problem is solved with the direct solver `UMFPACK64`.

Listing 2. The elasticity system.

```
load "UMFPACK64"
real sqrt2 = sqrt(2.0);
macro epsilon (u) [
  dx(u), dy(u#y), dz(u#z),
  (dz(u#y)+dy(u#z))/sqrt2,
  (dz(u)+dx(u#z))/sqrt2,
  (dy(u)+dx(u#y))/sqrt2] // EOM
problem elasticity(def(u), def(v), solver = "UMFPACK64")
  = int3d(Th)(la*chigamma*(div(u)*div(v)) + 2.0*mu*chigamma*(epsilon(u)'*epsilon(v)))
  - int3d(Th)(-chigamma*rho*gravity*vz) - int2d(Th, 2)(qx*v + qy*vy + qz*vz)
  + on(1, u = 0, uy = 0, uz = 0) + on(3, u = 0) + on(4, uy = 0);
```

The use of adaptive mesh refinement aims not only reducing the computational cost when compared to a structured mesh refinement over the whole hold-all domain, but also to achieve a final solution with an enhanced resolution. Whenever the optimality condition or the stopping criterion are fulfilled, an adaptive mesh refinement can be performed, as explained in Section 3.1. The basic idea consists in refining the mesh only in the region adjacent to the design domain Ω obtained in the previous iteration, while the region $\mathcal{D} \setminus \Omega$ filled with weak/light material phase remains with coarse elements. For such, we rely on the open-source library Mmg, which can be called from within FreeFEM. First `mshmet` saves the metric for the mesh `Th` and characteristic function `chi`. Then `Mmg3d` is called to read the metric and generating the new adapted mesh, as shown in the following Listing:

Listing 3. Adaptive mesh refinement.

```
load "mmg"
load "mshmet"
real[int] met=mshmet(Th, chi, hmin = Hmin, hmax = Hmax, err = Err);
Th=mmg3d(Th, metric=met, hausd = Hausd, hgrad = Hgrad);
```

The input parameters are listed as follows:

- `metric`: array to set or get metric data information;
- `hmin`, `hmax`: minimum and maximum edge size, respectively;
- `err`: interpolation error level, set as 0.01 by default;
- `hausd`: Hausdorff parameter to control boundary approximation, set as 0.01 by default;
- `hgrad`: parameter to set the gradation level, which controls the ratio between two adjacent edges. With a gradation of h, two adjacent edges l_1 and l_2 must respect that $1/h \leq l_1/l_2 \leq h$.

4. Numerical Experiments

In this section, three numerical experiments are presented to show the effectiveness of the proposed methodology. The minimization problem (3.8) is solved by using the topology optimization algorithm described in Section 3.1. In all numerical examples, the stopping criterion and the optimality threshold are set as $\epsilon_\kappa = 1.0 \times 10^{-3}$ and $\epsilon_\theta = 1^\circ$, respectively, and the parameter `eps` is set as the smallest edge of the mesh. In addition, the following material properties are assumed: Young's modulus $E = 210\ GPa$ and Poisson ratio $\nu = 1/3$. The body force $b = \delta b_0$, with δ given in (2.6) and $b_0 = -\rho_0 g e_3$, where $\rho_0 = 7.85 \times 10^3\ kg/m^3$, $g = 10\ m/s^2$ and e_i denotes the canonical basis of $\mathbb{R}^3$, with $i = 1, 2, 3$. In addition, since parameter δ_0 has been introduced to mimic voids, then it has to be set as small as possible. After performing an exhaustive numerical study, the material threshold was fixed as $\delta_0 = 10^{-6}$, which represents a good compromise in the sense that it does not contribute significantly neither to the stiffness nor to the weight of the resulting structure, but at the same time this value allows for keeping the stiffness matrix well conditioned. The surface traction q has intensity κq_0, where $q_0 = \rho_0 g\,|\mathcal{D}|$ and $0 \leq \kappa \leq 1$ is a rate parameter relating the surface traction intensity with the total weight of the hold-all structure. Moreover, the mechanical problem is discretized into linear tetrahedral finite elements. Finally, all numerical experiments were performed in a Windows Workstation with dual Intel Xeon Silver 4216 processor with a clock frequency of 2.10 GHz, having 16 cores in total and 96 GB of memory.

4.1. **Example 1.** In this example, the hold-all domain $\mathcal{D}$ is given by a prismatic block of $20 \times 5 \times 10\ m^3$, subject only to self-weight loading and fixed (clamped) in a small area of $5 \times 0.25\ m^2$ at the bottom of the two opposite sides, as shown in Figure 2.

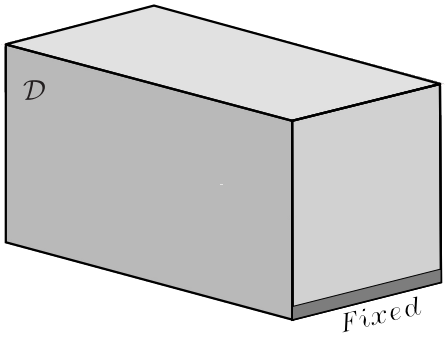

Figure 2. Example 1: Initial domain and boundary conditions.

For symmetry reasons, only one fourth of the domain is discretized in a structured mesh with 96,000 tetrahedral elements and 18,491 nodes. As previously mentioned, FreeFEM offers simple mesh generation functions, such as the command `cube`. For the sake of completeness, Listing 4 provides a simple implementation for generating and discretizing the initial design domain and also for imposing the labels associated with the desired boundary conditions regarding the elasticity problem.

Listing 4. Generating the initial discretized design domain.

```
include "cube.idp"
int n = 1; // mesh generation parameter
int[int] Nxyz1 = [10*n, 40*n, 1*n];
real [int, int] Bxyz1 = [[0.0, 02.5], [0., 10.0], [0., 0.25]];
int [int, int] Lxyz1 = [[4, 3], [1,3], [3,3]];
```

```
int[int] Nxyz2 = [10*n, 40*n, 39*n];
real [int, int] Bxyz2 = [[0.0, 2.5], [0.0, 1.0], [0.25, 1.0]];
int [int, int] Lxyz2 = [[4, 3], [3,5], [3,3]];
```

In this particular case, in which the structure is submitted only to self-weight loading, if we set $\alpha = 0$ the volume fraction converges to zero (that is, the standard compliance formulation is recovered). On the other hand, the volume fraction tends to increase for higher values of the parameter α. In fact, by setting $\alpha = 2.4$, the volume fraction goes to 100% for the present example. In this sense, in order to observe the role of the regularizing parameter α for the case of pure self-weight loading ($\kappa = 0$), we take it in the interval $0 \leq \alpha \leq 2.4$ to compute the associated volume fraction and relative compliance with respect of α. The obtained results are reported in the graph from Figure 3. As expected, in the interval $0 < \alpha < 2.4$, a family of non-trivial volume unconstrained solutions can be obtained, showing that the regularizing parameter α plays a fundamental role in the present context for imposing feasible volume fractions.

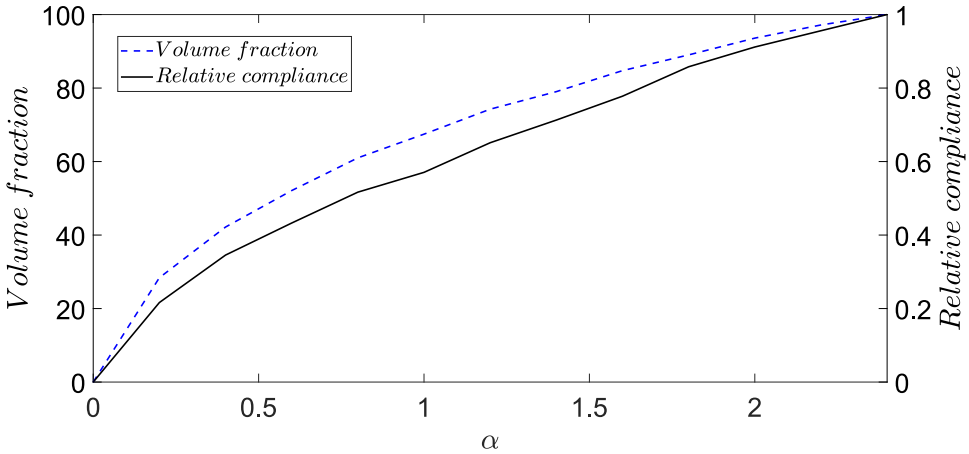

FIGURE 3. Example 1: Volume fraction and relative compliance for different values of the regularizing parameter α.

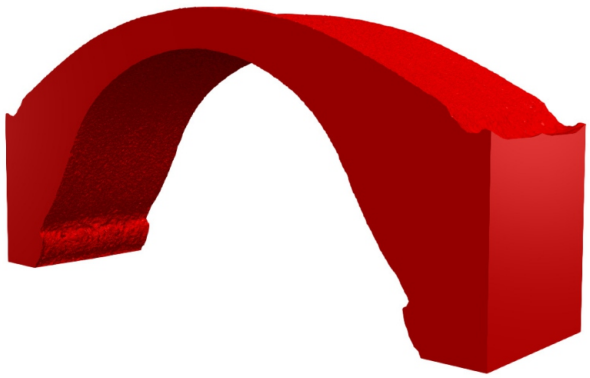

FIGURE 4. Example 1: Perspective view of the final topology.

Let us now select $\alpha = 0.45$, which leads to a volume fraction of 30%. The optimal solution is obtained after only 41 iterations and four adaptive mesh refinements. The final adapted mesh contains 3.224.566 elements and 547.147 nodes. Finally, the optimality condition is fulfilled with $\theta_{41} \approx 0°$. As previously mentioned, the use of adaptive mesh refinement aims to perform the topology optimization with a reduced computational cost and also to enhance the resolution of the optimal topology. In fact, for this particular example, the final topology is obtained after approximately 4 hours. Figure 5 illustrates how the mesh refinements increase the computational time for each iteration of optimization process, as the blue line becomes steeper after the adaptive mesh refinement procedures.

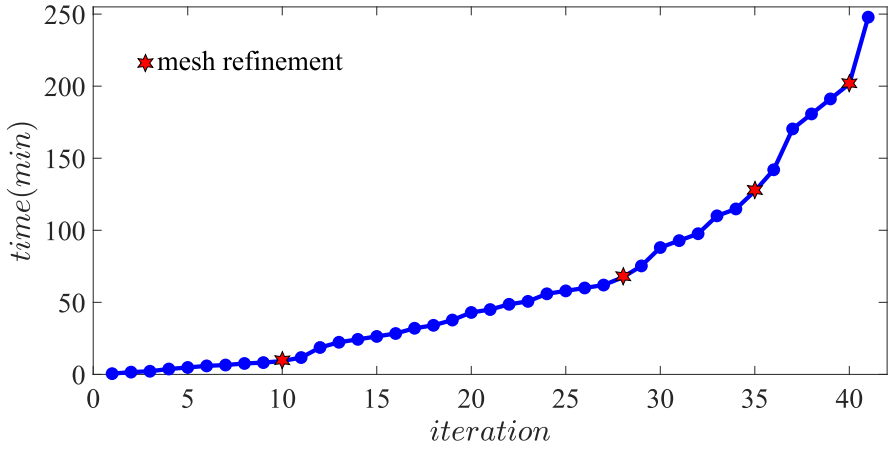

FIGURE 5. Example 2: Computational time during the iterative process.

Finally, the computational time for generating the new adapted meshes (see Listing 3) represents only a small fraction of the total computational time, as shown in Table 2. Therefore, the most expensive computational task of the FreeFEM implementation consists in solving the elasticity system, as expected.

TABLE 2. Computational time for generating the adapted meshes.

Mesh Refinement	Computational Time (s)
1^{st}	4.9
2^{nd}	18.2
3^{rd}	65.4
4^{th}	204.2

4.2. **Example 2.** Now, let us consider a hold-all domain given by a cube of dimensions $5 \times 5 \times 5\ m^3$ with hinge supports at the bottom, as shown in Figure 6. The cube is also subject to a surface traction $q = (\kappa q_0, 0, 0)\ N$ distributed in a small square region of dimensions $0.5 \times 0.5\ m^2$ at the center of the top face and acting in the horizontal direction, with the loading factor $\kappa = 0.4$. The hinge supports are also squares of dimension $0.25 \times 0.25\ m^2$ with their centers at $0.375\ m$ from the edges of the cube.

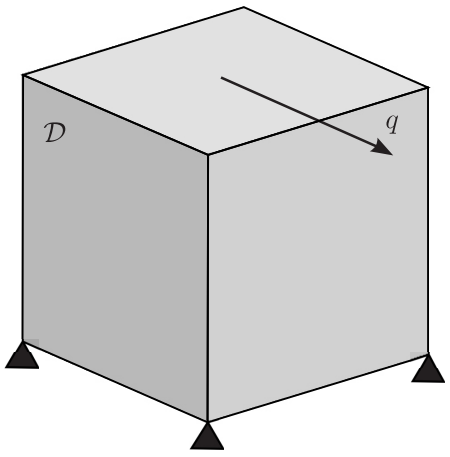

FIGURE 6. Example 2: Initial domain and boundary conditions.

In this example, two distinct cases are considered in the absence of regularizing parameter ($\alpha = 0$). The first one, referred to as Case 1, is free of self-weight loading whereas the second

case, named Case 2, takes into account the body force. In both cases, a volume fraction of 9% is imposed by linear penalization. For symmetry reasons, only one half of the domain is discretized in a structured mesh with 192,000 tetrahedral elements. At the end of the iterative process (in which three adaptive mesh refinements were performed for both cases), the final adapted mesh contains 2,793,143 elements and 472,570 nodes in Case 1 and 2,603,079 elements and 441,681 nodes in Case 2. Figure 7 shows the optimal topology obtained after 34 iterations for the case free of self-weight loading, in which the optimality condition is fulfilled with $\theta_{34} \approx 0.6°$. The final topology reported in Figure 8 for the scenario in which the body force is taken into account is obtained after 84 iterations, with the optimality condition also fulfilled, namely $\theta_{84} \approx 0.1°$.

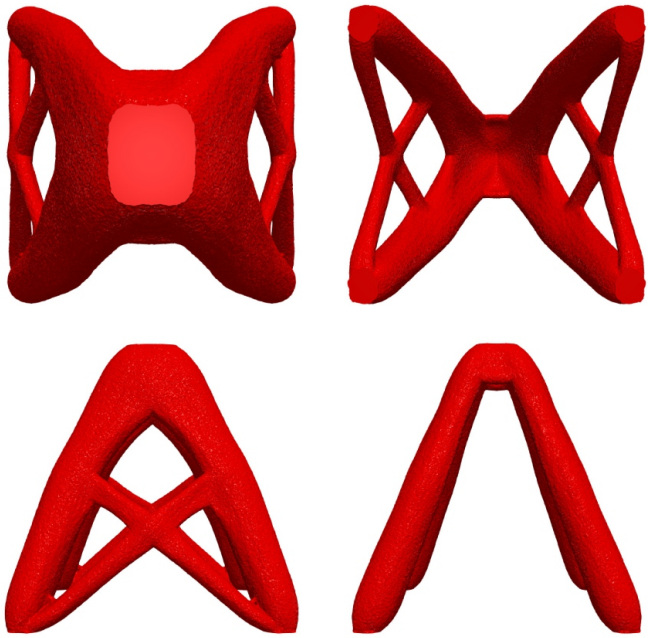

FIGURE 7. Example 2, Case 1: Top, bottom, side 1 and side 2 views of the final topology.

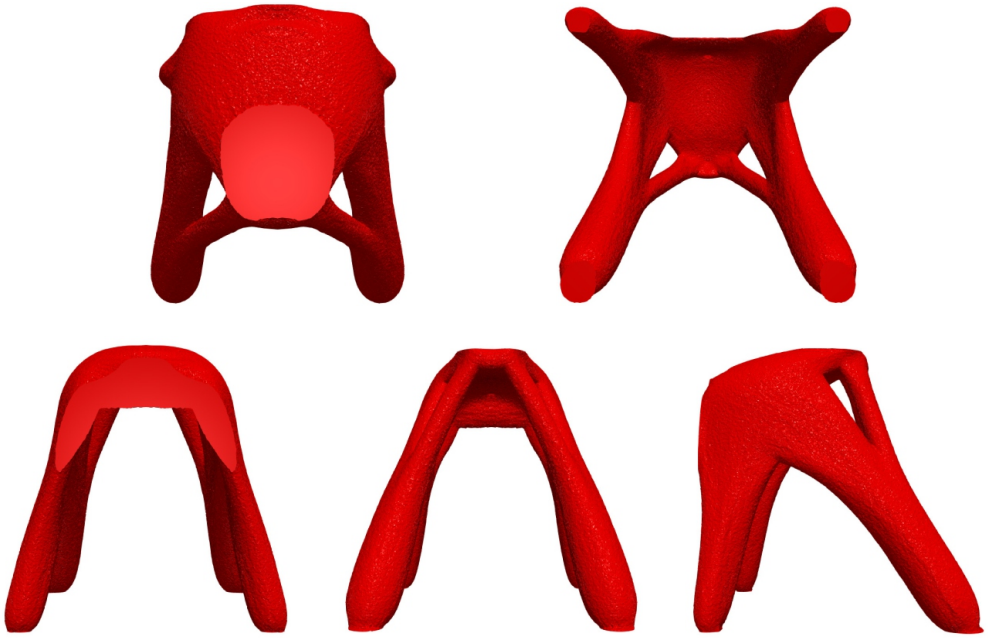

FIGURE 8. Example 2, Case 2: Top, bottom, side 1, side 2 and side 3 views of the final topology.

4.3. **Example 3.** Finally, let us consider the design of a tower by taking into account both external and body forces. The hold-all domain $\mathcal{D}$ is given by a prismatic block of dimensions

$120 \times 120 \times 300\ m^3$ fixed in small square areas of $3 \times 3\ m^2$ at the bottom of each side, as shown in Figure 9. The block is subject to a surface traction $q = (0, 0, -\kappa q_0)\ N$ distributed in a small square region of dimensions $0.6 \times 0.6\ m^2$ at the center of the top face and acting in the vertical direction, with the loading factor $\kappa = 0.02$.

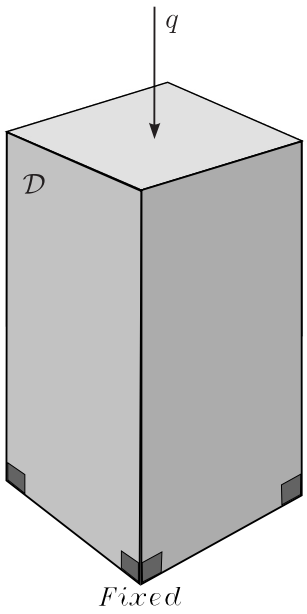

FIGURE 9. Example 3: Initial domain and boundary conditions.

Once more, only one fourth of the domain is discretized for symmetry reasons. The initial mesh contains 266.408 tetrahedral elements and 44.541 nodes, whereas at the end of the iterative process the final adapted mesh contains 1.983.117 elements and 335.129 nodes. In this particular example, the regularizing parameter is set as $\alpha = 0.06$, which leads to a volume fraction of approximately 9%. The optimality condition is fulfilled after five mesh refinements and 84 iterations, with $\theta_{84} \approx 0°$. The final topology is shown in Figures 10 and 11.

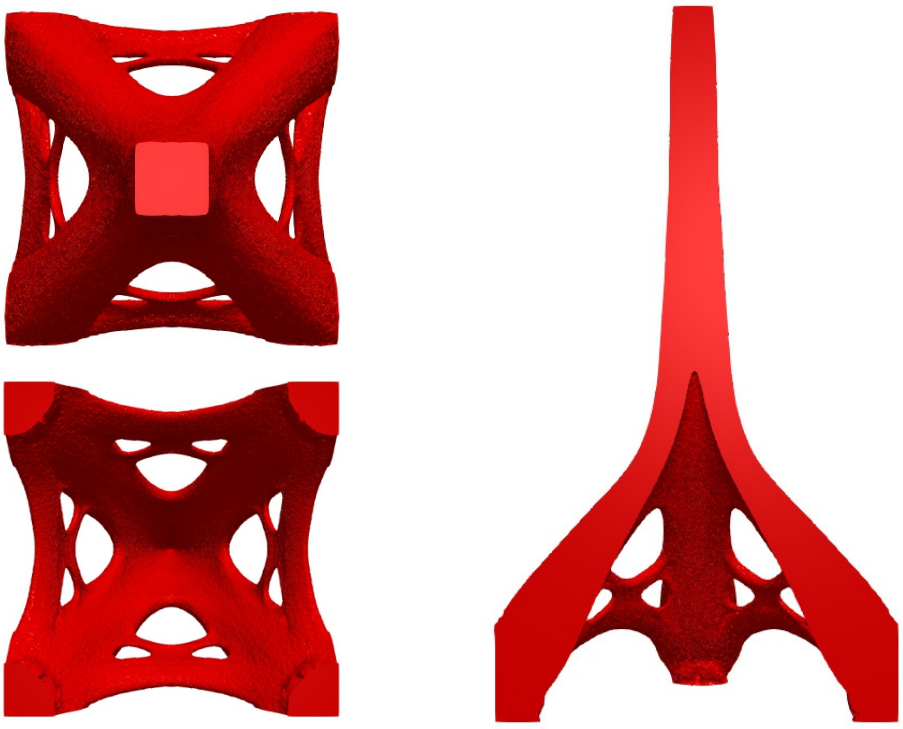

FIGURE 10. Example 3: Top, bottom and diagonal cut views of the final topology.

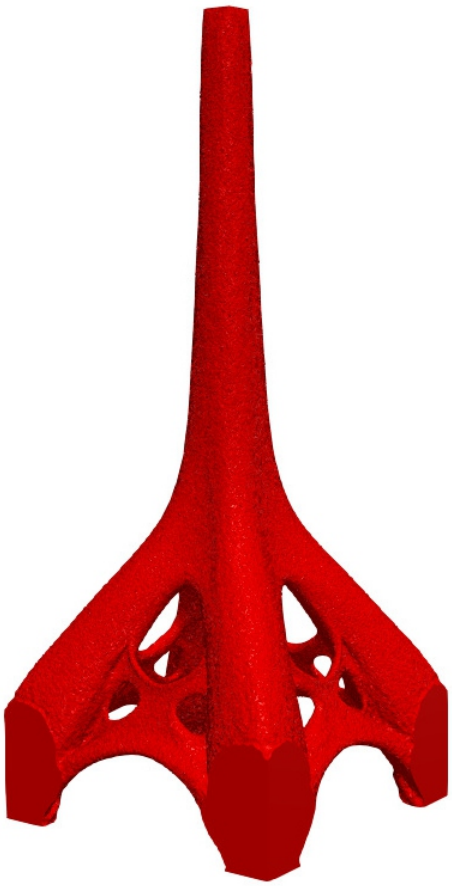

FIGURE 11. Example 3: Perspective view of the final topology.

5. Conclusions

We have considered the challenging problem regarding topology optimization of structures subject to self-weight loading. The main issue of such problem lies on the fact that the use of standard compliance minimization under volume constraint formulation leads to several difficulties already reported in the literature, such as non-monotonic behaviour of the compliance, possible unconstrained character of the optimum and parasitic effects for low densities in density-based approaches. Therefore, a regularized formulation of the classical compliance minimization problem which allows for imposing any feasible volume constraint has been adopted in order to overcome the first two difficulties. Besides, this regularized formulation also enjoys the important feature of recovering the standard (original) formulation once the regularizing parameter vanishes. In addition, the regularizing term is very simple and can be adopted in any other topology optimization method like the ones based on density models, including SIMP, for instance. The resulting topology optimization problem has been solved with the help of the topological derivative method, leading to a 0-1 topology optimization algorithm which naturally overcomes the last difficulty as no intermediate densities approach is necessary. Finally, in order to highlight the effectiveness of the proposed approach, a set of benchmark examples into three spatial dimensions has been presented, which are: a Roman-like bridge structure under pure self-weight loading (Example 1), a truss-like structure subject to both, self-weight loading and external forces acting co-linearly and in orthogonal directions (Example 2) and an Eiffel-like tower structure under external loads and dominant self-weight loading (Example 3). As a future work, we are interested in the multimaterial topology optimization of structures subject to self-weight loading, following the original ideas by Onco and Giusti (2020) and Gangl (2020), for instance.

Appendix A. Topological derivative of the compliance shape functional

Let us consider an open and bounded domain $\mathcal{D} \in \mathbb{R}^d$, with $d \geq 2$, which is subject to a non-smooth perturbation confined in a small ball-shaped region $B_\varepsilon(\hat{x})$ of radius ε and centre

at an arbitrary point $\hat{x}$ of $\mathcal{D}$, such that $\overline{B_\varepsilon(\hat{x})} \subset \mathcal{D}$. We introduce the characteristic function $x \mapsto \chi(x)$, $x \in \mathbb{R}^d$, associated with the unperturbed domain, namely $\chi := \mathbb{1}_{\mathcal{D}}$, such that

$$|\mathcal{D}| = \int_{\mathbb{R}^d} \chi \, , \tag{A.1}$$

where $|\mathcal{D}|$ is the Lebesgue measure of $\mathcal{D}$. Now, we define a characteristic function associated with the topologically perturbed domain of the form $x \mapsto \chi_\varepsilon(\hat{x};\ x)$, $x \in \mathbb{R}^d$. In the case of a perforation, for instance, $\chi_\varepsilon(\hat{x}) := \mathbb{1}_{\mathcal{D}} - \mathbb{1}_{B_\varepsilon(\hat{x})}$. Finally, we assume that the functional $\psi(\chi_\varepsilon(\hat{x}))$, associated with the topologically perturbed domain, admits a topological asymptotic expansion of the form

$$\psi(\chi_\varepsilon(\hat{x})) = \psi(\chi) + f(\varepsilon) D_T(\hat{x}) + o(f(\varepsilon)) \, , \tag{A.2}$$

where $\psi(\chi)$ is the shape functional associated with the unperturbed domain, $f(\varepsilon)$ is a positive function such that $f(\varepsilon) \to 0$ when $\varepsilon \to 0$, and $o(f(\varepsilon))$ is the remainder term, that is $o(f(\varepsilon))/f(\varepsilon) \to 0$ when $\varepsilon \to 0$. Function $\hat{x} \mapsto D_T\psi(\hat{x})$ is called the topological derivative of ψ at $\hat{x}$. Therefore, the product $f(\varepsilon) D_T\psi(\hat{x})$ represents a first order correction over $\psi(\chi)$ to approximate $\psi(\chi_\varepsilon(\hat{x}))$. In addition, after rearranging (A.2), we have

$$\frac{\psi(\chi_\varepsilon(\hat{x})) - \psi(\chi)}{f(\varepsilon)} = D_T\psi(\hat{x}) + \frac{o(f(\varepsilon))}{f(\varepsilon)} \, . \tag{A.3}$$

The limit passage $\varepsilon \to 0$ in the above expression leads to the general definition for the topological derivative, namely

$$D_T\psi(\hat{x}) := \frac{\psi(\chi_\varepsilon(\hat{x})) - \psi(\chi)}{f(\varepsilon)} \, . \tag{A.4}$$

Therefore, in order to evaluate the topological derivative of the compliance shape functional defined in (2.2), it is necessary to introduce the topologically perturbed counterpart of the problem. The idea consists in nucleating a spherical inclusion $B_\varepsilon(\hat{x})$ endowed with different material property from the background. In this case, $\chi_\varepsilon(\hat{x})$ is defined as $\chi_\varepsilon(\hat{x}) = \mathbb{1}_{\mathcal{D}} - (1 - \gamma)\mathbb{1}_{B_\varepsilon(\hat{x})}$, with the contrast γ defined as

$$\gamma = \gamma(x) := \begin{cases} \delta_0, & \text{if } x \in \Omega \, , \\ \delta_0^{-1}, & \text{if } x \in \mathcal{D} \setminus \Omega \, , \end{cases} \tag{A.5}$$

which allows us to induce a level-set domain representation method as presented in Section 3.1. From these elements, the following piece-wise constant function is introduced

$$\gamma_\varepsilon = \gamma_\varepsilon(x) := \begin{cases} 1, & \text{if } x \in \mathcal{D} \setminus \overline{B_\varepsilon(\hat{x})} \, , \\ \gamma, & \text{if } x \in B_\varepsilon(\hat{x}) \, . \end{cases} \tag{A.6}$$

Then, the compliance shape functional associated with the perturbed problem, denoted by $\mathcal{C}_\varepsilon(u_\varepsilon)$, is defined as

$$\mathcal{C}_\varepsilon(u_\varepsilon) = \int_{\mathcal{D}} b_\varepsilon \cdot u_\varepsilon + \int_{\Gamma_N} q \cdot u_\varepsilon \, , \tag{A.7}$$

where the vector function u_ε is the solution of the following variational problem: Find $u_\varepsilon \in \mathcal{U}$, such that

$$\int_{\mathcal{D}} \sigma_\varepsilon(u_\varepsilon) \cdot (\nabla\eta)^s = \int_{\mathcal{D}} b_\varepsilon \cdot \eta + \int_{\Gamma_N} q \cdot \eta \, , \quad \forall \eta \in \mathcal{V} \, , \tag{A.8}$$

with $\sigma_\varepsilon = \gamma_\varepsilon \sigma(u_\varepsilon)$, $b_\varepsilon = \gamma_\varepsilon b$ and γ_ε given by (A.6). The strong system associated with the variational problem (A.8) can be written as: Find u_ε, such that

$$\left\{ \begin{array}{rcll} \mathrm{div}\sigma_\varepsilon(u_\varepsilon) & = & b_\varepsilon & \text{in } \mathcal{D} \, , \\ \sigma_\varepsilon(u_\varepsilon) & = & \gamma_\varepsilon \delta \mathbb{C} (\nabla u_\varepsilon)^s & \\ u_\varepsilon & = & 0 & \text{on } \Gamma_D \, , \\ \sigma(u_\varepsilon) n & = & q & \text{on } \Gamma_N \, . \\ [\![u_\varepsilon]\!] & = & 0 & \left. \right\} \text{on } \partial B_\varepsilon \, , \\ [\![\sigma_\varepsilon(u_\varepsilon)]\!] n & = & 0 & \left. \right\} \end{array} \right. \tag{A.9}$$

where the operator $[\![\varphi]\!]$ denotes the jump of function φ on the boundary of the inclusion ∂B_ε, i.e., $[\![\varphi]\!] := \varphi_{|_{\mathcal{D}\setminus\overline{B_\varepsilon}}} - \varphi_{|_{B_\varepsilon}}$ on ∂B_ε, see Figure 12. The transmission conditions on the interface ∂B_ε comes out naturally from the variational formulation (A.8), namely $[\![u_\varepsilon]\!] = 0$ and $[\![\sigma_\varepsilon(u_\varepsilon)]\!] n = 0$.

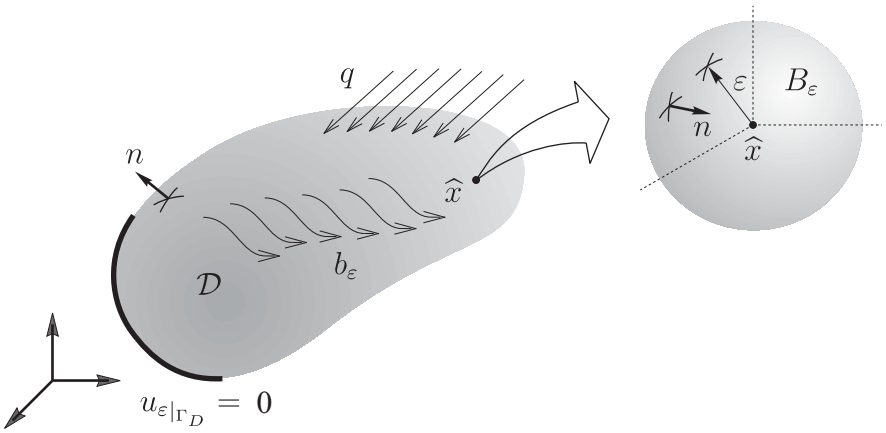

FIGURE 12. The elasticity problem defined in the perturbed domain.

In order to simplify further analysis, let us introduce an auxiliary vector function v, which is the solution of the following adjoint variational problem: Find $v \in \mathcal{V}$, such that

$$\int_{\mathcal{D}} \sigma(v) \cdot (\nabla \eta)^s = -\int_{\mathcal{D}} b \cdot \eta - \int_{\Gamma_N} q \cdot \eta \quad \forall \eta \in \mathcal{V} \,, \tag{A.10}$$

with $\sigma(v) = \delta\mathbb{C}(\nabla v)^s$. Note that, in this particular case, the problem is self-adjoint in the sense that, by comparing the adjoint equation (A.10) with the state equation (2.3), we conclude that $v = -u$, provided that $\mathcal{U} = \mathcal{V}$ according to (2.5).

A.1. **Existence of the topological derivative.** The existence of the associated topological derivative is ensured by the following result:

Lemma 2. *Let u and u_ε be the solutions of the original* (2.3) *and perturbed* (A.8) *problems, respectively. Then, the following estimates holds true:*

$$\|u_\varepsilon - u\|_{H^1(\mathcal{D})} \leq C\varepsilon^{3/2} \,, \tag{A.11}$$

where C is a constant independent of the small parameter ε.

Proof. From the definition of the contrast γ_ε given by (A.6), we may rewrite (2.3) as

$$\int_{\mathcal{D}\setminus\overline{B_\varepsilon}} \sigma(u) \cdot (\nabla\eta)^s + \int_{B_\varepsilon} \sigma(u) \cdot (\nabla\eta)^s \pm \int_{B_\varepsilon} \gamma\sigma(u) \cdot (\nabla\eta)^s = \int_{\mathcal{D}\setminus\overline{B_\varepsilon}} b \cdot \eta + \int_{B_\varepsilon} b \cdot \eta \pm \int_{B_\varepsilon} \gamma b \cdot \eta + \int_{\Gamma_N} q \cdot \eta \,. \tag{A.12}$$

or even as

$$\int_{\mathcal{D}} \sigma_\varepsilon(u) \cdot (\nabla\eta)^s + (1-\gamma)\int_{B_\varepsilon} \sigma(u) \cdot (\nabla\eta)^s = \int_{\mathcal{D}} b_\varepsilon \cdot \eta + (1-\gamma)\int_{B_\varepsilon} b \cdot \eta + \int_{\Gamma_N} q \cdot \eta \,. \tag{A.13}$$

Now, by taking $\eta = v_\varepsilon := u_\varepsilon - u$ as a test function in the above equation and also in (A.8), it follows that

$$\int_{\mathcal{D}} \sigma_\varepsilon(u) \cdot (\nabla v_\varepsilon)^s = \int_{\mathcal{D}} b_\varepsilon \cdot v_\varepsilon + \int_{\Gamma_N} q \cdot v_\varepsilon + (1-\gamma)\int_{B_\varepsilon} b \cdot v_\varepsilon - (1-\gamma)\int_{B_\varepsilon} \sigma(u) \cdot (\nabla v_\varepsilon)^s \,, \tag{A.14}$$

$$\int_{\mathcal{D}} \sigma_\varepsilon(u_\varepsilon) \cdot (\nabla v_\varepsilon)^s = \int_{\mathcal{D}} b_\varepsilon \cdot v_\varepsilon + \int_{\Gamma_N} q \cdot v_\varepsilon \,, \tag{A.15}$$

After subtracting the first equation from the second one, we obtain the following equality:

$$\int_{\mathcal{D}} \sigma_\varepsilon(v_\varepsilon) \cdot (\nabla v_\varepsilon)^s = (1-\gamma)\int_{B_\varepsilon} (\sigma(u) \cdot (\nabla v_\varepsilon)^s - b \cdot v_\varepsilon) \,. \tag{A.16}$$

From the Cauchy-Schwarz inequality, there is

$$\begin{aligned}\int_{\mathcal{D}} \sigma_\varepsilon(v_\varepsilon)\cdot(\nabla v_\varepsilon)^s &\leq C_1\|\sigma(u)\|_{L^2(B_\varepsilon)}\|(\nabla v_\varepsilon)^s\|_{L^2(B_\varepsilon)} + C_2\|b\|_{L^2(B_\varepsilon)}\|v_\varepsilon\|_{L^2(B_\varepsilon)}\\ &\leq C_3\varepsilon^{3/2}\|v_\varepsilon\|_{H^1(\mathcal{D})}\,, \end{aligned} \tag{A.17}$$

where we have used the interior elliptic regularity of u and the continuity of function b at the point $\hat{x}$. In addition, from the coercivity of the bilinear form of the left-hand side of (A.17), namely

$$c\|v_\varepsilon\|^2_{H^1(\mathcal{D}} \leq \int_{\mathcal{D}} \sigma_\varepsilon(v_\varepsilon)\cdot(\nabla v_\varepsilon)^s\,, \tag{A.18}$$

we have

$$\|v_\varepsilon\|^2_{H^1(\mathcal{D})} \leq C\varepsilon^{3/2}\|v_\varepsilon\|_{H^1(\mathcal{D})}\,, \tag{A.19}$$

which leads to the result with $C = C_3/c$ and $v_\varepsilon = u_\varepsilon - u$. □

A.2. **Topological asymptotic analysis.** Now, with the aid of the adjoint equation (A.10) and some manipulation, it is possible to write variation of the shape functional in terms of an integral concentrated in the ball B_ε. In fact, by subtracting (2.2) from (A.7) and from the definition of the contrast γ_ε in (A.6), it follows that

$$\begin{aligned}\mathcal{C}_\varepsilon(u_\varepsilon) - \mathcal{C}(u) &= \int_{\mathcal{D}}(b_\varepsilon\cdot u_\varepsilon - b\cdot u) + \int_{\Gamma_N} q\cdot(u_\varepsilon - u)\\ &= -(1-\gamma)\int_{B_\varepsilon} b\cdot u_\varepsilon + \int_{\mathcal{D}} b\cdot(u_\varepsilon - u) + \int_{\Gamma_N} q\cdot(u_\varepsilon - u)\,. \end{aligned} \tag{A.20}$$

The state equation associated with the topologically perturbed problem (A.8) may be rewritten as

$$\begin{aligned}\int_{\mathcal{D}\setminus\overline{B_\varepsilon}} \sigma(u_\varepsilon)\cdot(\nabla\eta)^s + \int_{B_\varepsilon}\gamma\sigma(u_\varepsilon)\cdot(\nabla\eta)^s \pm \int_{B_\varepsilon}\sigma(u_\varepsilon)\cdot(\nabla\eta)^s =\\ \int_{\mathcal{D}\setminus\overline{B_\varepsilon}} b\cdot\eta \int_{B_\varepsilon}\gamma b\cdot\eta \pm \int_{B_\varepsilon} b\cdot\eta\int_{\Gamma_N} q\cdot\eta\,, \end{aligned} \tag{A.21}$$

where we have used the definition of the contrast γ_ε given in (A.6). Then, we have that

$$\int_{\mathcal{D}}\sigma(u_\varepsilon)\cdot(\nabla\eta)^s = \int_{\mathcal{D}} b\cdot\eta + (1-\gamma)\int_{B_\varepsilon}\sigma(u_\varepsilon)\cdot(\nabla\eta)^s - (1-\gamma)\int_{B_\varepsilon} b\cdot\eta + \int_{\Gamma_N} q\cdot\eta\,. \tag{A.22}$$

Now, by subtracting the state equation associated with the unperturbed problem (2.2) from the above result, it follows that

$$\int_{\mathcal{D}}\sigma(u_\varepsilon - u)\cdot(\nabla\eta)^s = (1-\gamma)\int_{B_\varepsilon}\sigma(u_\varepsilon)\cdot(\nabla\eta)^s - (1-\gamma)\int_{B_\varepsilon} b\cdot\eta\,. \tag{A.23}$$

By taking $\eta = v$ as a test function in the above equation, where v is the solution of the adjoint problem (A.10), we have

$$\int_{\mathcal{D}}\sigma(u_\varepsilon - u)\cdot(\nabla v)^s = (1-\gamma)\int_{B_\varepsilon}\sigma(u_\varepsilon)\cdot(\nabla v)^s - (1-\gamma)\int_{B_\varepsilon} b\cdot v\,. \tag{A.24}$$

On the other hand, by setting $\eta = u_\varepsilon - u$ as a test function in the adjoint equation (A.10), there is

$$\int_{\mathcal{D}}\sigma(v)\cdot\nabla(u_\varepsilon - u)^s = -\int_{\mathcal{D}} b\cdot(u_\varepsilon - u) - \int_{\Gamma_N} q\cdot(u_\varepsilon - u)\,. \tag{A.25}$$

Since the bilinear forms on the left-hand side of the above two last equations are symmetric, we obtain:

$$\int_{\mathcal{D}} b\cdot(u_\varepsilon - u) + \int_{\Gamma_N} q\cdot(u_\varepsilon - u) = (1-\gamma)\int_{B_\varepsilon}\sigma(u_\varepsilon)\cdot(\nabla v)^s + (1-\gamma)\int_{B_\varepsilon} b\cdot v\,. \tag{A.26}$$

By adding the term

$$-(1-\gamma)\int_{B_\varepsilon} b\cdot u_\varepsilon \tag{A.27}$$

on both sides of the above expression, there is

$$\int_{\mathcal{D}} b\cdot(u_\varepsilon-u)-(1-\gamma)\int_{B_\varepsilon} b\cdot u_\varepsilon+\int_{\Gamma_N} q\cdot(u_\varepsilon-u)=(1-\gamma)\int_{B_\varepsilon}\sigma(u_\varepsilon)\cdot(\nabla v)^s \\ -(1-\gamma)\int_{B_\varepsilon} b\cdot u_\varepsilon+(1-\gamma)\int_{B_\varepsilon} b\cdot v\;, \quad \text{(A.28)}$$

and then comparing it with (A.20), we conclude that

$$\mathcal{C}_\varepsilon(u_\varepsilon)-\mathcal{C}(u)=\frac{1-\gamma}{\gamma}\int_{B_\varepsilon}\sigma_\varepsilon(u_\varepsilon)\cdot(\nabla u)^s-(1-\gamma)\int_{B_\varepsilon} b\cdot(u_\varepsilon+u)\;, \quad \text{(A.29)}$$

where we have used the fact that $v=-u$ for the particular case associated with the compliance shape functional (see comment just after (A.10)).

The variation of the compliance shape functional has been written exclusively in terms of integrals concentrated in the ball B_ε, as shown through (A.29). In order to obtain the associated topological asymptotic expansion in the form of (A.2), we need to know the asymptotic behaviour of the solution u_ε with respect to ε in the neighborhood of the ball B_ε. In this sense, let us propose an *ansatz* for u_ε in the form

$$u_\varepsilon(x)=u(x)+w_\varepsilon(x)+\tilde{u}_\varepsilon(x)\;, \quad \text{(A.30)}$$

where u is the solution of the unperturbed problem (2.3), w_ε is the solution of an exterior problem yet to be defined and $\tilde{u}_\varepsilon$ is a remainder. After applying the operator $\sigma_\varepsilon=\gamma_\varepsilon\sigma$ on the ansatz (A.30), we have

$$\begin{aligned}\sigma_\varepsilon(u_\varepsilon(x)) &= \sigma_\varepsilon(u(x))+\sigma_\varepsilon(w_\varepsilon(x))+\sigma_\varepsilon(\tilde{u}_\varepsilon(x)) \\ &= \gamma_\varepsilon\sigma(u(\hat{x}))+\gamma_\varepsilon(\sigma(u(x))-\sigma(u(\hat{x})))+\sigma_\varepsilon(w_\varepsilon(x))+\sigma_\varepsilon(\tilde{u}_\varepsilon(x))\;. \quad \text{(A.31)}\end{aligned}$$

On the boundary of the inclusion ∂B_ε there is

$$[\![\sigma_\varepsilon(u_\varepsilon)]\!]n=0 \quad \Rightarrow \quad (\sigma(u_\varepsilon)_{|_{\mathcal{D}\setminus\overline{B_\varepsilon}}}-\gamma\sigma(u_\varepsilon)_{|_{B_\varepsilon}})n=0\;, \quad \text{(A.32)}$$

so that the above expansion evaluated on ∂B_ε yields

$$(1-\gamma)\sigma(u(\hat{x}))n+(1-\gamma)(\sigma(u(x))-\sigma(u(\hat{x})))n+[\![\sigma_\varepsilon(w_\varepsilon(x))]\!]n+[\![\sigma_\varepsilon(\tilde{u}_\varepsilon(x))]\!]n=0\;, \quad \text{(A.33)}$$

which allows us for choosing the jump $[\![\sigma_\varepsilon(w_\varepsilon(x))]\!]n$ on ∂B_ε as

$$[\![\sigma_\varepsilon(w_\varepsilon(x))]\!]n=-(1-\gamma)\sigma(u(\hat{x}))n\;. \quad \text{(A.34)}$$

Now, the following exterior problem is formally defined with $\varepsilon\to 0$: Find $\sigma_\varepsilon(w_\varepsilon)$, such that

$$\left\{\begin{array}{rcll}\mathrm{div}\sigma_\varepsilon(w_\varepsilon) &=& 0 & \text{in } \mathbb{R}^3\;,\\ \sigma_\varepsilon(w_\varepsilon) &\to& 0 & \text{at } \infty\;,\\ [\![\sigma_\varepsilon(w_\varepsilon)]\!]n &=& \hat{\varphi} & \text{on } \partial B_\varepsilon\;,\end{array}\right. \quad \text{(A.35)}$$

where $\hat{\varphi}=-(1-\gamma)\sigma(u(\hat{x}))n$. The above boundary value problem admits an explicit solution. In addition, once the solution of the exterior problem (A.35) is uniform inside the inclusion $B_\varepsilon(\hat{x})$, it means that the stress acting in the inclusion embedded in the whole three-dimensional space $\mathbb{R}^3$ may be written in the following compact form:

$$\sigma_\varepsilon(w_\varepsilon(x))_{|_{B_\varepsilon(\hat{x})}}=\gamma\mathbb{T}\sigma(u(\hat{x}))\;, \quad \text{(A.36)}$$

where $\mathbb{T}$ is a fourth order uniform (constant) tensor given by

$$\mathbb{T}=(3\alpha_2-1)\mathbb{I}+(\alpha_1-\alpha_2)\mathrm{I}\otimes\mathrm{I}\;, \quad \text{(A.37)}$$

in which the constants α_1 and α_2 are given by

$$\alpha_1=\frac{1-\nu}{3(1-\nu)-(1+\nu)(1-\gamma)} \quad \text{and} \quad \alpha_2=\frac{5(1-\nu)}{15(1-\nu)-(8-10\nu)(1-\gamma)}\;. \quad \text{(A.38)}$$

Now, we proceed with the construction of the remainder $\tilde{u}_\varepsilon$ in such a way that it compensates for the discrepancies introduced by the higher order terms in ε as well as by the boundary layer

w_ε on the exterior boundary $\partial\mathcal{D}$. Thus, the remainder $\tilde{u}_\varepsilon$ has to be the solution of the following boundary value problem: Find $\tilde{u}_\varepsilon$, such that

$$\left\{\begin{array}{rcll} \mathrm{div}\sigma_\varepsilon(\tilde{u}_\varepsilon) &=& 0 & \text{in } \mathcal{D}\ , \\ \sigma_\varepsilon(\tilde{u}_\varepsilon) &=& \gamma_\varepsilon\delta\mathbb{C}(\nabla\tilde{u}_\varepsilon)^s & \\ \tilde{u}_\varepsilon &=& f_\varepsilon & \text{on } \Gamma_D\ , \\ \sigma(\tilde{u}_\varepsilon)n &=& g_\varepsilon & \text{on } \Gamma_N\ . \\ [\![\tilde{u}_\varepsilon]\!] &=& 0 \ \Big\} & \\ [\![\sigma_\varepsilon(\tilde{u}_\varepsilon)]\!]n &=& h_\varepsilon \ \Big\} & \text{on } \partial B_\varepsilon\ , \end{array}\right. \tag{A.39}$$

where $f_\varepsilon = -w_{\varepsilon|_{\Gamma_D}}$, $g_\varepsilon = -\sigma(w_\varepsilon)n_{|_{\Gamma_N}}$ and $h_\varepsilon = \tilde{\sigma}n$ with the second order tensor field $\tilde{\sigma}(x) = -(1-\gamma)[\sigma(u(x)) - \sigma(u(\hat{x}))]$. The remainder $\tilde{u}_\varepsilon$ enjoys the asymptotic behaviour of the form $\|\tilde{u}_\varepsilon\|_{H_1(\mathcal{D})} = O(\varepsilon^3)$. The proof is completely analogous to the one obtained in the two spatial dimensions case in (Novotny and Sokołowski, 2020, Chapter 5).

We may now proceed to the topological derivative evaluation. From the contrast (A.6) and the ansatz (A.30), the first integral of the right-hand side of (A.29) may be rewritten as

$$\int_{B_\varepsilon}\sigma_\varepsilon(u_\varepsilon)\cdot(\nabla u)^s = \underbrace{\int_{B_\varepsilon}\sigma_\varepsilon(u)\cdot(\nabla u)^s}_{(a)} + \underbrace{\int_{B_\varepsilon}\sigma_\varepsilon(w_\varepsilon)\cdot(\nabla u)^s}_{(b)} + \mathcal{E}_1(\varepsilon)\ . \tag{A.40}$$

The remainder $\mathcal{E}_1(\varepsilon)$ is defined as

$$\begin{aligned} \mathcal{E}_1(\varepsilon) &= \int_{B_\varepsilon}\sigma_\varepsilon(\tilde{u}_\varepsilon)\cdot(\nabla u)^s\ , \\ |\mathcal{E}_1(\varepsilon)| &\le \|\sigma_\varepsilon(\tilde{u}_\varepsilon)\|_{L^2(B_\varepsilon)}\|(\nabla u)^s\|_{L^2(B_\varepsilon)} \\ &\le C_1\varepsilon^{3/2}\|\tilde{u}_\varepsilon\|_{H^1(\mathcal{D})} \le C_2\varepsilon^{9/2} = O(\varepsilon^{9/2})\ , \end{aligned} \tag{A.41}$$

where we have used the Cauchy-Schwarz inequality together with the already known estimate for $\tilde{u}_\varepsilon$. Now, from the term (a) in (A.40), there is

$$\begin{aligned} \int_{B_\varepsilon}\sigma_\varepsilon(u(x))\cdot(\nabla u(x))^s &= \int_{B_\varepsilon}\gamma(\sigma(u(x))\cdot(\nabla u(x))^s \pm \sigma(u(\hat{x}))\cdot(\nabla u(\hat{x}))^s) \\ &= \frac{4}{3}\pi\varepsilon^3\gamma\sigma(u(\hat{x}))\cdot(\nabla u(\hat{x}))^s + \mathcal{E}_2(\varepsilon)\ , \end{aligned} \tag{A.42}$$

where the remainder $\mathcal{E}_2(\varepsilon)$ is given by

$$\begin{aligned} \mathcal{E}_2(\varepsilon) &= \int_{B_\varepsilon}(h(x) - h(\hat{x}))\ , \\ |\mathcal{E}_2(\varepsilon)| &\le C_3\|h(x) - h(\hat{x})\|_{L^2(B_\varepsilon)}\|1\|_{L^2(B_\varepsilon)} \\ &\le C_4\varepsilon^{3/2}\|x - \hat{x}\|_{L^2(B_\varepsilon)} \le C_5\varepsilon^4 = O(\varepsilon^4)\ , \end{aligned} \tag{A.43}$$

with $h(x) - h(\hat{x}) = \gamma(\sigma(u(x))\cdot(\nabla u(x))^s - \sigma(u(\hat{x}))\cdot(\nabla u(\hat{x}))^s)$. Once again, the Cauchy-Schwarz inequality was applied together with the interior elliptic regularity of u. Since the exact solution of the exterior problem (A.35) is explicitly known, the term (b) from (A.40) can be written as

$$\begin{aligned} \int_{B_\varepsilon}\sigma_\varepsilon(w_\varepsilon)\cdot(\nabla u)^s &= \int_{B_\varepsilon}(\sigma(w_\varepsilon)\cdot(\nabla u(x))^s \pm \sigma_\varepsilon(w_\varepsilon)\cdot(\nabla u(\hat{x}))^s) \\ &= (\nabla u(\hat{x}))^s\cdot\int_{B_\varepsilon}\sigma_\varepsilon(w_\varepsilon) + \int_{B_\varepsilon}\sigma_\varepsilon(w_\varepsilon)\cdot((\nabla u(x))^s - (\nabla u(\hat{x}))^s) \\ &= \frac{4}{3}\pi\varepsilon^3\gamma\mathbb{T}\sigma(u(\hat{x}))\cdot(\nabla u(\hat{x}))^s + \mathcal{E}_3(\varepsilon)\ , \end{aligned} \tag{A.44}$$

where the remainder $\mathcal{E}_3(\varepsilon)$ is defined as

$$\begin{aligned} \mathcal{E}_3(\varepsilon) &= \int_{B_\varepsilon}\sigma_\varepsilon(w_\varepsilon)\cdot((\nabla u(x))^s - (\nabla u(\hat{x}))^s)\ , \\ |\mathcal{E}_3(\varepsilon)| &\le \|\sigma_\varepsilon(w_\varepsilon)\|_{L^2(B_\varepsilon)}\|(\nabla u(x))^s - (\nabla u(\hat{x}))^s\|_{L^2(B_\varepsilon)} \le C_6\varepsilon^4 = O(\varepsilon^4)\ , \end{aligned} \tag{A.45}$$

where we have used the interior elliptic regularity of function u once again and the fact that $\sigma_\varepsilon(w_\varepsilon)$ is uniform in $B_\varepsilon(\hat{x})$.

Now, after replacing the expansion (A.30) in the second term on the right-hand side of (A.29), it follows that

$$\int_{B_\varepsilon} b\cdot(u_\varepsilon+u) = 2\underbrace{\int_{B_\varepsilon} b\cdot u}_{(a)} + \underbrace{\int_{B_\varepsilon} b\cdot(u_\varepsilon-u)}_{(b)}\,, \tag{A.46}$$

For the term (a) in (A.46), there is

$$\begin{aligned}\int_{B_\varepsilon} b(x)\cdot u(x) &= \int_{B_\varepsilon}(b(x)\cdot u(x)\pm b(\hat{x})\cdot u(\hat{x}))\\ &= \frac{4}{3}\pi\varepsilon^3 b(\hat{x})\cdot u(\hat{x})+\mathcal{E}_4(\varepsilon)\,,\end{aligned} \tag{A.47}$$

with the remainder $\mathcal{E}_4(\varepsilon)$ defined as

$$\begin{aligned}\mathcal{E}_4(\varepsilon) &= \int_{B_\varepsilon}(b(x)\cdot u(x)-b(\hat{x})\cdot u(\hat{x}))\,,\\ |\mathcal{E}_4(\varepsilon)| &\le \|b(x)\cdot u(x)-b(\hat{x})\cdot u(\hat{x})\|_{L^2(B_\varepsilon)}\|1\|_{L^2(B_\varepsilon)}\\ &\le C_7\varepsilon^{3/2}\|x-\hat{x}\|_{L^2(B_\varepsilon)}\le C_8\varepsilon^4 = O(\varepsilon^4)\,,\end{aligned} \tag{A.48}$$

where we have used the Cauchy-Schwarz inequality together with the interior elliptic regularity of function u. The term (b) in (A.46) can be estimated by using the Cauchy-Schwarz inequality and Lemma 2 as follows

$$\begin{aligned}\mathcal{E}_5(\varepsilon) &= \int_{B_\varepsilon} b\cdot(u_\varepsilon-u)\,,\\ |\mathcal{E}_5(\varepsilon)| &\le \|b\|_{L^2(B_\varepsilon)}\|u_\varepsilon-u\|_{L^2(B_\varepsilon)}\\ &\le C_9\varepsilon^{3/2+\delta}\|u_\varepsilon-u\|_{H^1(\mathcal{D})}\le C_{10}\varepsilon^{3+\delta}=o(\varepsilon^3)\,,\end{aligned} \tag{A.49}$$

with $0<\delta<1$, where we have used the Hölder inequality together with the Sobolev embedding theorem. For more details, see (Novotny and Sokołowski, 2020, Section 1.2.2).

Now, let us come back to the expansion (A.29), which from all the above elements may be rewritten as

$$\mathcal{C}_\varepsilon(u_\varepsilon)-\mathcal{C}(u) = \frac{4}{3}\pi\varepsilon^3[\mathbb{P}_\gamma\sigma(u(\hat{x}))\cdot(\nabla u(\hat{x}))^s - 2(1-\gamma)b(\hat{x})\cdot u(\hat{x})] + \sum_{i=1}^{5}\mathcal{E}_i(\varepsilon)\,, \tag{A.50}$$

where $\mathbb{P}_\gamma = (1-\gamma)(\mathbb{I}+\mathbb{T})$ is a fourth order isotropic tensor obtained from Bonnet and Delgado (2013), namely

$$\mathbb{P}_\gamma = (1-\gamma)[3\alpha_2\mathbb{I}+(\alpha_1-\alpha_2)\mathrm{I}\otimes\mathrm{I}]\,. \tag{A.51}$$

For more details, see also Ammari and Kang (2007); Ammari et al. (2013b). From the expansion (A.50), we may promptly identify the function $f(\varepsilon)=\frac{4}{3}\pi\varepsilon^3$, which allows us to obtain the following topological derivative formula for the compliance shape functional

$$D_T\mathcal{C}(\hat{x}) = \mathbb{P}_\gamma\sigma(u(\hat{x}))\cdot(\nabla u(\hat{x}))^s - 2(1-\gamma)b(\hat{x})\cdot u(\hat{x})\,. \tag{A.52}$$

Finally, the results reported in Theorem 1 are obtained after replacing γ by δ_0 according to (A.5) and then taking the limit $\delta_0\to 0$.

Funding

This research was partly supported by CNPq (Brazilian Research Council), CAPES (Brazilian Higher Education Staff Training Agency) and FAPERJ (Research Foundation of the State of Rio de Janeiro). These supports are gratefully acknowledged.

Conflict of interest

The authors declare that they have no conflict of interest.

Replication of results

The authors state that all the data necessary to replicate the results are presented in the manuscript.

References

H. Ammari and H. Kang. *Reconstruction of small inhomogeneities from boundary measurements.* Lectures Notes in Mathematics vol. 1846. Springer-Verlag, Berlin, 2004.

H. Ammari and H. Kang. *Polarization and moment tensors with applications to inverse problems and effective medium theory.* Applied Mathematical Sciences vol. 162. Springer-Verlag, New York, 2007.

H. Ammari, J. Garnier, W. Jing, H. Kang, M. Lim, K. Sølna, and H. Wang. *Mathematical and statistical methods for multistatic imaging*, volume 2098. Springer, Switzerland, 2013a.

H. Ammari, H. Kang, K. Kim, and H. Lee. Strong convergence of the solutions of the linear elasticity and uniformity of asymptotic expansions in the presence of small inclusions. *Journal of Differential Equations*, 254(12):4446–4464, 2013b.

S. Amstutz. Analysis of a level set method for topology optimization. *Optimization Methods and Software*, 26(4-5):555–573, 2011.

S. Amstutz. An introduction to the topological derivative. *Engineering Computations*, 39(1): 3–33, 2022.

S. Amstutz and H. Andrä. A new algorithm for topology optimization using a level-set method. *Journal of Computational Physics*, 216(2):573–588, 2006.

R. Ansola, J. Canales, and J. A. Tárrago. An efficient sensitivity computation strategy for the evolutionary structural optimization (eso) of continuum structures subjected to self-weight loads. *Finite Elements in Analysis and Design*, 42:1220–1230, 2006.

G. Barros, J. Filho, L. Nunes, and M. Xavier. Experimental validation of a topological derivative-based crack growth control method using digital image correlation. *Engineering Computations*, 39(1):438–454, 2022.

Ph. Baumann and K. Sturm. Adjoint-based methods to compute higher-order topological derivatives with an application to elasticity. *Engineering Computations*, 39(1):60–114, 2022.

M. P. Bendsøe and N. Kikuchi. Generating optimal topologies in structural design using an homogenization method. *Computer Methods in Applied Mechanics and Engineering*, 71(2): 197–224, 1988.

M. Bonnet. On the justification of topological derivative for wave-based qualitative imaging of finite-sized defects in bounded media. *Engineering Computations*, 39(1):313–336, 2022.

M. Bonnet and G. Delgado. The topological derivative in anisotropic elasticity. *The Quarterly Journal of Mechanics and Applied Mathematics*, 66(4):557–586, 2013.

M. Bruyneel and P. Duysinx. Note on topology optimization of continuum structures including self-weight. *Structural and Multidisciplinary Optimization*, 29:245–256, 2005.

A. Canelas and J.R. Roche. Shape and topology optimal design problems in electromagnetic casting. *Engineering Computations*, 39(1):147–171, 2022.

C. Chang and A. Chen. The gradient projection method for structural topology optimization including density-dependent force. *Structural and Multidisciplinary Optmimization*, 50:645–657, 2014.

M. Dalla Riva, M.L. de Cristoforis, and P. Musolino. *Singularly perturbed boundary value problems: A functional analytic approach.* Springer Nature Switzerland, 2021.

M.C. Delfour. Topological derivatives via one-sided derivative of parametrized minima and minimax. *Engineering Computations*, 39(1):34–59, 2022.

L. Fernandez and R. Prakash. Imaging of small penetrable obstacles based on the topological derivative method. *Engineering Computations*, 39(1):201–231, 2022.

A. Ferrer and S.M. Giusti. Inverse homogenization using the topological derivative. *Engineering Computations*, 39(1):337–353, 2022.

J. M. M. Luz Filho, R. Mattoso, and L. Fernandez. A freefem code for topological derivative-based structural optimization. *Structural and Multidisciplinary Optimization*, 66(74), 2023. doi: 10.1007/s00158-023-03529-5.

P. Gangl. A multi-material topology optimization algorithm based on the topological derivative. *Computer Methods in Applied Mechanics and Engineering*, 366:113090, 2020.

A. Garaigordobil, R. Ansola, J. Canales, and R. Borinaga. Addressing topology optimization with overhang constraints for structures subject to self-weight loads. *Structural and Multidisciplinary Optimization*, 65:358, 2022.

S. Garreau, Ph. Guillaume, and M. Masmoudi. The topological asymptotic for PDE systems: the elasticity case. *SIAM Journal on Control and Optimization*, 39(6):1756–1778, 2001.

F. Hecht. FreeFEM documentation. https://doc.freefem.org/introduction/index.html. Accessed in August 2022.

X. Huang and Y.M. Xie. Evolutionary topology optimization of continuum structures including design-dependent self-weight loads. *Finite Elements in Analysis and Design*, 47:942–948, 2011.

Ph. Kliewe, A. Laurain, and K. Schmidt. Shape optimization in acoustic-structure interaction. *Engineering Computations*, 39(1):172–200, 2022.

P. Kumar. Topology optimization of stiff structures under self-weight for given volume using a smooth heaviside function. *Structural and Multidisciplinary Optimization*, 65:128, 2022.

F. Le Louër and M.L. Rapún. Topological sensitivity analysis revisited for time-harmonic wave scattering problems. Part I: The free space case. *Engineering Computations*, 39(1):232–271, 2022a.

F. Le Louër and M.L. Rapún. Topological sensitivity analysis revisited for time-harmonic wave scattering problems. Part II: Recursive computations by the boundary integral equation method. *Engineering Computations*, 39(1):272–312, 2022b.

V. G. Maz'ya, S. A. Nazarov, and B. A. Plamenevskij. *Asymptotic theory of elliptic boundary value problems in singularly perturbed domains. Vol. I*, volume 111 of *Operator Theory: Advances and Applications*. Birkhäuser Verlag, Basel, 2000. Translated from the German by Georg Heinig and Christian Posthoff.

A.A. Novotny and J. Sokołowski. *An introduction to the topological derivative method*. Springer Briefs in Mathematics. Springer Nature Switzerland, 2020. doi: 10.1007/978-3-030-36915-6.

A.A. Novotny, C.G. Lopes, and R.B. Santos. Topological derivative-based topology optimization of structures subject to self-weight loading. *Structural and Multidisciplinary Optimization*, 63: 1853–1861, 2021. doi: 10.1007/s00158-020-02780-4.

A.A. Novotny, S.M. Giusti, and S. Amstutz. Guest Editorial: On the topological derivative method and its applications in computational engineering. *Engineering Computations*, 39(1): 1–2, 2022.

A. A. R. Onco and S. M. Giusti. A robust topological derivative-based multi-material optimization approach: optimality condition and computational algorithm. *Computer Methods in Applied Mechanics and Engineering*, 366:113044, 2020. doi: 10.1016/j.cma.2020.113044.

L. Rakotondrainibe, G. Allaire, and P. Orval. Topological sensitivity analysis with respect to a small idealized bolt. *Engineering Computations*, 39(1):115–146, 2022.

A. Romero. Optimum design of two-material bending plate compliant devices. *Engineering Computations*, 39(1):395–420, 2022.

R.B. Santos and C.G. Lopes. Topology optimization of structures subject to self-weight loading under stress constraints. *Engineering Computations*, 39(1):380–394, 2022.

J. Sokołowski and A. Żochowski. On the topological derivative in shape optimization. *SIAM Journal on Control and Optimization*, 37(4):1251–1272, 1999.

M. Xavier and N. Van Goethem. Brittle fracture on plates governed by topological derivatives. *Engineering Computations*, 39(1):421–437, 2022.

H. Xu, L. Guan, X. Chen, and L. Wang. Guide-weight method for topology optimization of continuum structures including body forces. *Finite Elements in Analysis and Design*, 75: 38–49, 2013.

R. Yera, L. Forzani, C.G. Méndez, and A.E. Huespe. A topology optimization algorithm based on topological derivative and level-set function for designing phononic crystals. *Engineering Computations*, 39(1):354–379, 2022.

(J. M. M. Luz Filho and A. A. Novotny) Laboratório Nacional de Computação Científica LNCC/MCTI, Coordenação de Métodos Matemáticos e Computacionais, Av. Getúlio Vargas 333, 25651-075 Petrópolis - RJ, Brasil

Email address: novotny@lncc.br